remote sensing

MDPI

Article

Estimation of Land Deformation and Groundwater Storage Dynamics in Shijiazhuang–Baoding–Cangzhou–Hengshui Using Multi-Temporal Interferometric Synthetic Aperture Radar

Qiuhong Yang [1], Xing Zhang [1], Jun Hu [1,2], Rong Gui [1,*] and Liuming Yang [3]

[1] School of Geosciences and Info-Physics, Central South University, Changsha 410083, China
[2] Hunan Geological Disaster Monitoring, Early Warning and Emergency Rescue Engineering Technology Research Center, Changsha 410004, China
[3] College of Geographic Science, Hunan Normal University, Changsha 410081, China
* Correspondence: ronggui@csu.edu.cn

Abstract: Groundwater resources are crucial to socio-economic development and the ecosystem, and over-extraction can cause the groundwater level to drop, deplete reserves, and trigger geological hazards like land subsidence. The North China Plain (NCP) has experienced both subsidence and groundwater depletion due to over-extraction in the past 70 years. In this study, we used MT-InSAR technology and ascending C-band Sentinel-1 SAR data from 2017 to 2023 to study land deformation in the junction area of Shijiazhuang–Baoding–Cangzhou–Hengshui. We identified multiple subsidence funnels with a maximum rate exceeding −150 mm/year and a total deformation surpassing 600 mm. Seasonal decomposition methods accurately separated seasonal signals in the time-series deformation and groundwater level data. An exponential function model applied to long-term deformation showed no significant decrease in subsidence in severely affected areas. By modeling seasonal deformation and seasonal groundwater levels, we determined the elastic skeletal storage coefficients (S_{ke}) to be in the range of 1.02×10^{-3}~6.53×10^{-3} in subsidence areas. We obtained the spatiotemporal evolution of the total groundwater storage (TGWS), irreversible ground storage (IGWS), and recoverable ground storage (RGWS). The TGWS and IGWS decreased annually while the RGWS increased, which is attributable to the implementation of the South-to-North Water Diversion Project (SNWDP) and the issuance of groundwater withdrawal policies in the NCP.

Keywords: land deformation; elastic skeletal storage coefficient; groundwater storage; time-series displacements; groundwater level; North China Plain

Citation: Yang, Q.; Zhang, X.; Hu, J.; Gui, R.; Yang, L. Estimation of Land Deformation and Groundwater Storage Dynamics in Shijiazhuang–Baoding–Cangzhou–Hengshui Using Multi-Temporal Interferometric Synthetic Aperture Radar. *Remote Sens.* **2024**, *16*, 1724. https://doi.org/10.3390/rs16101724

Academic Editor: Michele Saroli

Received: 22 March 2024
Revised: 24 April 2024
Accepted: 11 May 2024
Published: 13 May 2024

1. Introduction

Groundwater resources are crucial to socio-economic development and the ecosystem, and over-extraction can cause the groundwater level to drop, deplete reserves, and trigger geological hazards like land subsidence. Both large urban areas and the basins with intensive agricultural planting have experienced severe land subsidence due to excessive groundwater extraction [1–9], especially in the NCP [10–16]. The NCP is one of the areas with the greatest shortage of water resources and prominent environmental problems in China. The groundwater supply in the NCP has reached 70% of the total water supply. The groundwater has experienced a long-term overexploitation process and has formed several large composite water level depression funnels, which have induced a large area of rapid land subsidence, becoming the area with the largest subsidence area and the most complex types in China. Land subsidence in the NCP first began in the 1920s and entered a stage of rapid development from the mid-1960s to the mid-1980s. From 1971 to 2015, the area of the North China Plain with an average annual subsidence greater than 20 mm was

48,500 square kilometers [10]. Uneven ground subsidence not only causes severe damage to above-ground buildings and underground pipeline facilities but also poses a serious threat to the safe operation of major infrastructures such as highways and high-speed railways. Moreover, it can lead to geological disasters like ground collapses and fissures. At the same time, areas with severe ground subsidence are prone to flooding disasters. The continuous development of ground subsidence disasters in the NCP has greatly affected and restricted local sustainable economic construction. Therefore, to prevent and control geological disasters caused by ground subsidence in the NCP, it is urgent to clarify the spatiotemporal evolution pattern of ground subsidence and unravel the coupling relationship between confined water changes and ground subsidence.

Traditional methods of surface deformation monitoring, such as GNSS and leveling, are often limited by high observation costs, small working ranges, and low spatial resolution. These constraints result in local and discrete measurements that struggle to accurately reflect the macroscopic details of real surface deformation fields. This impacts the accuracy and reliability of settlement monitoring. However, spaceborne synthetic aperture radar (InSAR) interferometry has emerged as a highly effective technique for measuring deformation in spatially dense surface domains. With its low cost, large range, and high spatial resolution advantages, InSAR has proven particularly useful in hydrology and groundwater extraction processes.

In 2001, Bawden researchers utilized time-series InSAR technology to detect the effects of groundwater pumping and discovered lateral contraction in the Southern California faults, which effectively showcased InSAR's potential for precise monitoring of hydrological activities [17]. Subsequently, numerous scholars have extensively utilized InSAR technology for monitoring areas of groundwater extraction [18–23]. Furthermore, by utilizing area monitoring data from InSAR technology and water head data, the water storage parameters of the aquifer system and time lag can be estimated [24–27]. More importantly, the long-term InSAR data can also measure seasonal changes due to the yearly cycle of groundwater pumping and recharge, as well as ongoing subsidence from continuous aquifer overdrafts [28–30]. In recent years, numerous scholars have carried out a series of studies in the NCP using time-series InSAR technology and obtained good results, albeit concentrated in major city such as Beijing, Cangzhou and Tianjin [31–34]. In agricultural areas, attention is only paid to ground subsidence, without in-depth research on the relationship between aquifer inversion and deformation. Additionally, from Taihang Mountain to Bohai Bay, the alluvial plain can be sequentially divided into the Piedmont plain (PP), flood plain (FP) and coast plain (CP), with significant differences in hydrogeological conditions. Therefore, it is crucial to conduct comprehensive research on land subsidence and aquifer inversion in different plain areas.

In this study, we took the over-extraction of confined groundwater and severe ground subsidence in the junction area of Shijiazhuang, Baoding, Cangzhou and Hengshui cities as our research area. Utilizing Sentinel-1A data from 2017 to 2023 to monitor the spatiotemporal distribution characteristics of the surface deformation, combined with water head data to analyze the different responses of aquifer systems to changes in the water head. Furthermore, according to the coupling relationship between the seasonal components of confined groundwater and surface deformation, the elastic skeletal storage coefficients and annual total groundwater storage (TGWS), irreversible ground storage (IGWS), and recoverable ground storage (RGWS) were determined, and we analyzed their spatiotemporal evolution laws.

2. Study Region and Data

2.1. Study Region

The NCP is a typical alluvial plain, formed by the massive sedimentation of silt brought by the Yellow River, Hai River, Huai River, and Luan River. The thickness of the sediment reaches 700 to 800 meters. From Taihang Mountain to Bohai Bay, the alluvial plain can be sequentially divided into the Piedmont plain (PP), flood plain (FP) and coast plain

(CP). The aquifer is the Quaternary aquifer group in the NCP, with a thickness of 350–500 m, which can be divided into four aquifer groups. Groundwater extraction is located in the second and third aquifers, at depths of 120–170 m and 250–310 m, respectively. Due to excessive groundwater extraction, the North China Plain has become the largest subsidence funnel area in the world.

The study area in this paper is located in the junction area of Shijiazhuang, Baoding, Cangzhou, and Hengshui cities (hereafter referred to simply as "AOI") in the NCP, which has serious subsidence, including the Piedmont plain and flood plain, as shown in Figure 1. The groundwater exploitation in the AOI area began in the late 1970s. As the regional economy rapidly developed, the water demand for agricultural irrigation increased sharply, the mining output volume continued to expand, and the water level dropped rapidly year by year. By 2015, the total decline in the central water level exceeded 64 m, forming a deep confined groundwater funnel with an area of 1600 km^2 [10]. The long-term continuous exploitation of confined groundwater led to serious land subsidence, with a subsidence rate of up to 100 mm/yr. To safeguard groundwater resources and mitigate land subsidence disasters, the SNWDP was implemented, and the groundwater level in the North China Plain was restored at a rate of 1–2 m/yr.

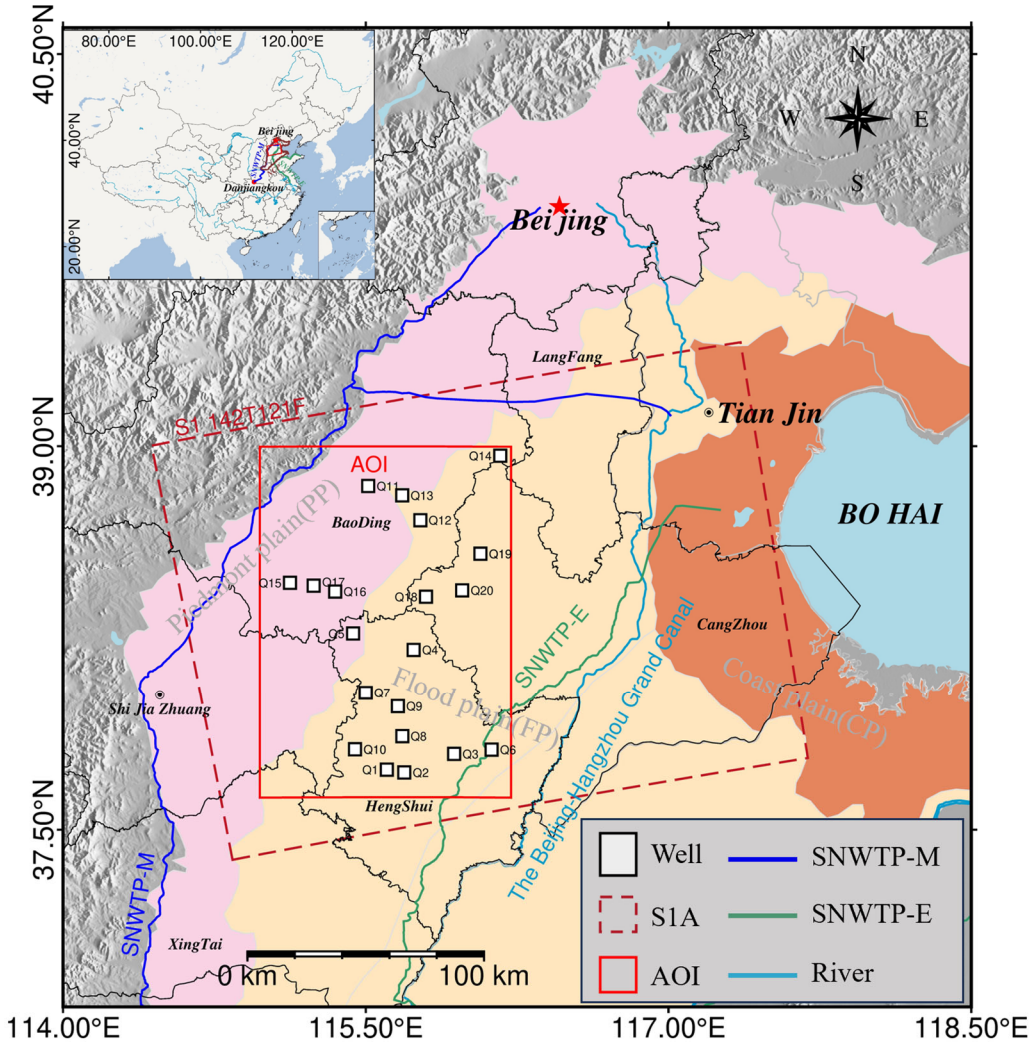

Figure 1. Study region (AOI) and the SAR data coverage (pink: Piedmont plain (PP), yellow: flood plain (FP), orange: coast plain (CP)).

2.2. Data

2.2.1. InSAR Datasets

The SAR data used in this article were collected from 20 May 2017 to 22 September 2023, totaling 187 scenes of Sentinel-1A ascending orbit data and the parameters of SAR data, as shown in Table 1. The band used was the C-band, with VV polarization. The azimuth and range resolutions were, respectively, 20 m and 5 m. The width of the SAR data was 250 km, and a region of interest (AOI) measuring 150 km × 130 km has been selected within it. Its coverage area is shown in Figure 1. In addition, this paper used SRTM DEM data with a resolution of 30 m covering the experimental area to remove the terrain phase in interferograms and perform geographic coding.

Table 1. The parameters of Sentinel-1 data.

Sensor	Band	Wavelength (cm)	Incidence Angle (°)	Heading (°)	Track	Polarization	Pass Direction	Number of Images	Date Range
S1	C	5.6	39.3	−12.9	142	VV	Ascending	187	20/05/2017–22/09/2023

2.2.2. Hydraulic Head

This article collected monthly monitoring data from 20 pressurized groundwater head observation wells in the research area from Jan. 2018 to Oct. 2022 (Figure 1), which were used to analyze the response relationship between ground subsidence and water head changes and to calculate the aquifer parameters. The recorded depths of all the wells, ranging from 130 to 210 m, indicate that groundwater is extracted from deep confined aquifers.

3. Method

In this section, we initially apply the MT-InSAR algorithm to determine the time-series deformation of the AOI region. Following that, we employ a seasonal separation algorithm to distinguish between periodic and long-term deformations. By integrating groundwater level data, we derive estimates for both the aquifer and GWS parameters. The process is illustrated in Figure 2.

3.1. Time-Series InSAR Data Processing

In this study, we used time-series SBAS InSAR technology to solve the problems of incoherence caused by crop growth changes in agricultural areas and the scarcity of artificial target points, achieving high-precision surface deformation measurement in the AOI areas. Next, we will provide a brief introduction to this method.

First, to mitigate noise impact, we applied a multi-look process on each SAR dataset at a 10:2 ratio (range/azimuth). Second, to counteract decorrelation from extensive time/space baselines, we established a spatial baseline of 150 m and a temporal baseline limit of 36 days. We then computed the average coherence for each interferometric pair and selected 406 pairs based on their quality and coherence for time-series analysis. The specific baseline combination is depicted in Figure 3. Then, SRTM DEM and orbit data were used to remove the terrain phase from the interferograms, and the Goldstein filtering method was used to further improve coherence. The minimum cost flow (MCF) method was used for phase unwrapping, and finally, the unwrapped differential interferograms were geocoded.

The SBAS InSAR method utilizes time-series analysis of high-coherence point targets. To enhance the computational efficiency and result reliability, we established a coherence threshold of 0.5 for selecting these points [35,36]. We then carried out DEM error elimination and atmospheric delay correction on the selected points. This paper estimated removal based on the linear relationship between the DEM error and vertical baseline [37]. The atmospheric signals on each interferogram were corrected using the Generic Atmospheric Correction Online Service for InSAR products [38]. Secondly, we performed secondary processing on the residual atmospheric phase. Due to the flatness of our region of interest

(AOI), the vertical layering in atmospheric delay had the least impact on deformation monitoring. Therefore, we used polynomial fitting to remove the phase trend of the interference pattern for the atmospheric delay of long-wave signals. This step could also eliminate orbital trends. Lastly, we set up a linear model linking the interference phase with unknown parameters to derive the LOS average deformation rate and time-series results using the SVD method. Ground subsidence due to groundwater overexploitation primarily stems from vertical deformation with minor horizontal shifts [39]. Hence, this study focused on investigating vertical deformations within our AOI region.

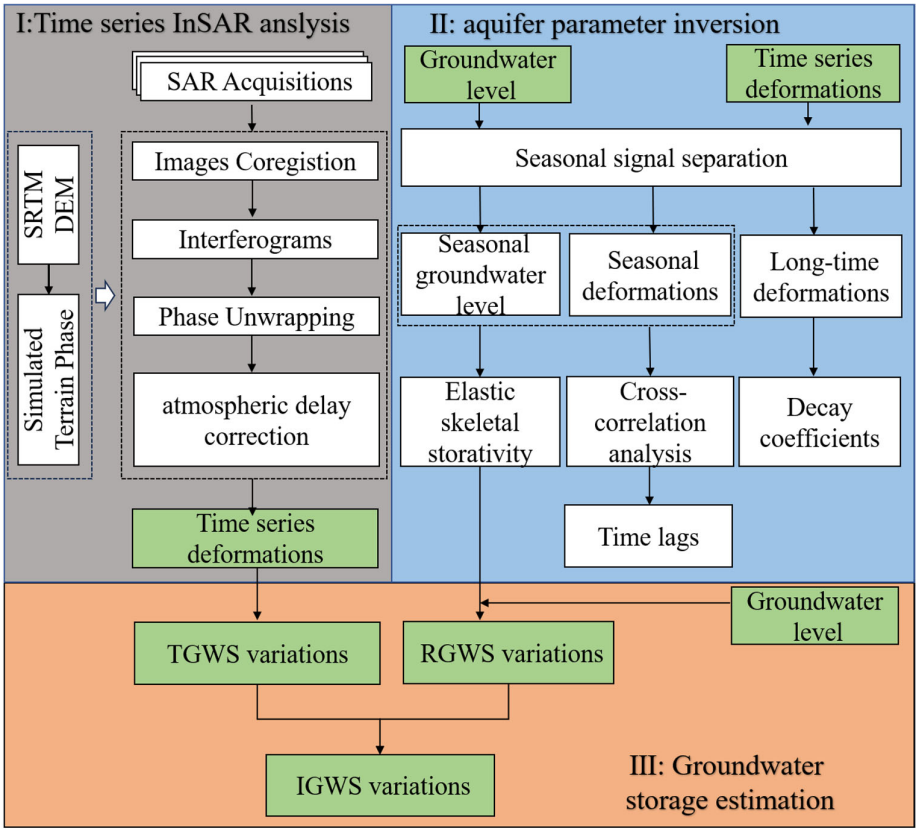

Figure 2. Flowchart of the data-processing procedure.

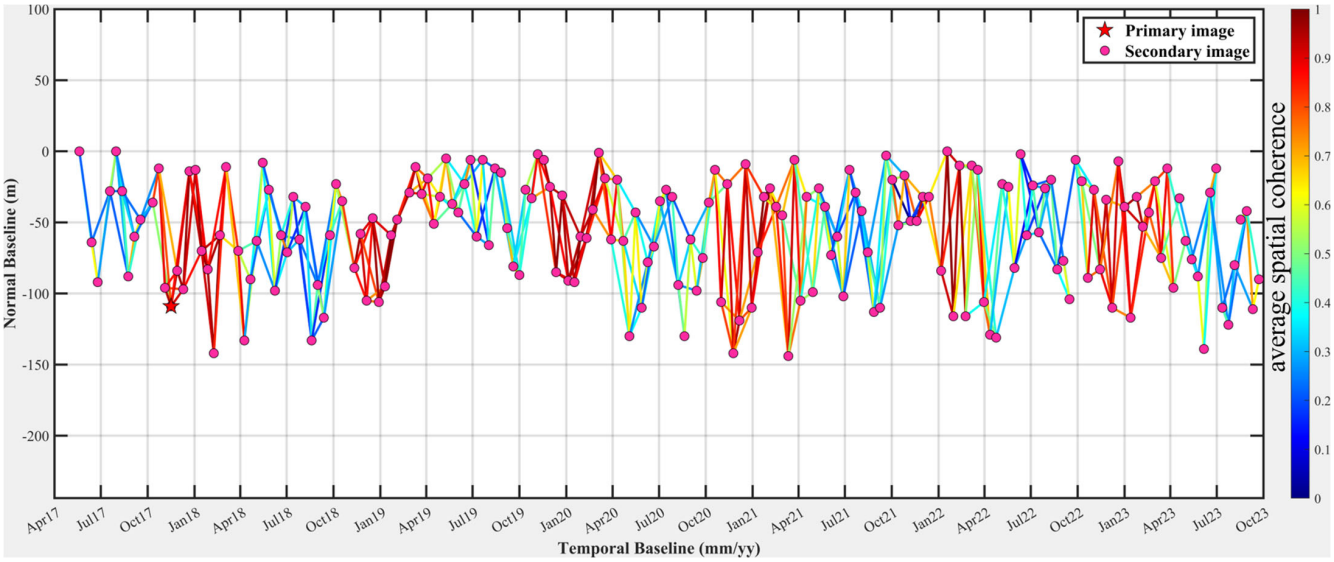

Figure 3. Temporal/perpendicular baseline for the Sentinel-1A interferometric pairs.

3.2. Aquifer Parameter Inversion

In order to obtain the elastic release coefficient of the AOI aquifer, this paper adopts the single sinusoid model as follows to separate the seasonal and long-term trends of temporal deformation and groundwater level data, respectively:

$$Y(t) = vt + Acos(2\pi(t - T)) + B \tag{1}$$

where $Y(t)$ are the time series of deformation and head, v are the average rates of deformation and head, A is the seasonal variation amplitude, t is the time, T is the moment when the seasonal signals reach a peak, and B is a constant term.

Seasonal deformation is caused by seasonal changes in groundwater levels, but due to the presence of heterogeneous permeable media in the aquifer, seasonal deformation often lags behind changes in groundwater levels. Therefore, to accurately determine the relationship between groundwater and seasonal deformation, it is necessary to estimate the lag time of deformation relative to the groundwater levels. The following formula can be used to conduct a correlation analysis of the time-series deformation and groundwater level.

$$\tau_{lag} = \text{argmax}(corr(\Delta h_{detrend}(t), \Delta b_{detrend}(t + \tau))) \tag{2}$$

where τ_{lag} is the time for seasonal deformation to lag head changes, $corr$ is the coherence coefficient, $\Delta b_{detrend}$ is the seasonal deformation time series after removing the linear trend, and $\Delta h_{detrend}$ is the seasonal head change time series after removing the linear trend. When conducting coherence analysis, due to the different time resolutions between the two, seasonal deformation interpolation is required to obtain deformation results corresponding to the observation time of the groundwater level. The results of this step are also applicable to the inversion of aquifer parameters.

The permanent loss of groundwater reserves leads to irreversible compaction of the aquifer, resulting in long-term trend deformation, also known as inelastic deformation. It takes several decades or even hundreds of years for long-term trend deformation to stabilize. In order to further explore its temporal evolution, we used the exponential function [23,40] to model and analyze it.

$$def(t) = M(e^{kt} - 1) \tag{3}$$

where $def(t)$ is the vertical deformation time series, M is the value that characterizes the cumulative displacement, and $k \in [-1, 0]$ The closer the k value is to -1, the faster the land subsidence rate slows down. The closer the k value is to 0, the slower the subsidence rate slows down.

The confined aquifer system consists of a weak permeable layer and an aquifer. The S_{ke} coefficients represent the strength of the aquifer's water release capacity, which can be estimated based on the linear relationship between the thickness of the aquifer and the groundwater level. However, due to the difficulty of directly measuring the preconsolidation head and the changes that may occur with groundwater extraction and replenishment, it poses difficulties in solving the aquifer parameters. In 2015, Shirazaei proposed a method for estimating aquifer parameters based on seasonal deformation and head changes, which solved the above problem [41]. The water release coefficient of the elastic skeleton can be solved using the following formula:

$$S_{ke} = \frac{\Delta d_s}{\Delta h_s} \tag{4}$$

where Δd_s represents the seasonal variation of aquifer thickness, i.e., the seasonal deformation, and Δh_s represents the seasonal variation of the water head.

3.3. Aquifer Groundwater Storage (GWS) Estimation

The change in the groundwater storage is a direct characterization of the activity of confined aquifers. The change in the total groundwater storage is a product of the interaction between natural recharge and artificial overexploitation and compaction in the

aquifer system. It can be obtained by multiplying the total vertical surface deformation with the aquifer area. The formula is as follows:

$$\Delta V = \Delta V_r + \Delta V_i = \Delta d_t \cdot A \tag{5}$$

where ΔV is the TWGS change, ΔV_r is the RGWS change, ΔV_i is the IGWS change, Δd_t is the total vertical cumulative deformation, and A is the area of the aquifer.

The TWGS change can be obtained by multiplying the elastic release coefficient with the total groundwater level change.

$$\Delta V_r = S_{ke} \cdot \Delta h_t \cdot A \tag{6}$$

where Δh_t is the total groundwater level change.

$$\Delta V_i = \Delta V - \Delta V_r = (\Delta d_t \cdot A) - (S_{ke} \cdot \Delta h_t \cdot A) \tag{7}$$

According to Formulas (6) and (7), the IGWS is equal to the TGWS change minus the RGWS change, and we can accurately calculate the permanent loss in the AOI area.

4. Results

4.1. Land Deformation Monitoring Results and Analysis

The results of the AOI regional surface deformation monitoring from 2017 to 2023 are shown in Figure 4a. Ground subsidence is widely distributed, especially in the southern part, which has now connected with the Handan subsidence area. The maximum subsidence rate can reach up to 15 cm/year. This region, a crop cultivation area, primarily experiences land subsidence due to the ongoing compaction of the aquifer system due to excessive extraction of confined groundwater. To further analyze the spatiotemporal distribution of the AOI regional subsidence funnels, we conducted profile extraction across multiple subsidence funnels (A–B profile), as shown in Figure 4b. Within six years, subsidence has been intensifying and the maximum cumulative deformation has reached 650 mm, meaning all the subsidence funnels will merge into one large super-subsiding funnel zone. Overexploitation of confined groundwater primarily causes ground subsidence due to the continuous compaction of the aquifer. To better understand how the aquifer system responds to changes in the groundwater level, this article compares the deformation time series of the groundwater level changes in six typical observation wells and their nearby InSAR monitoring points, and the results are shown in Figure 5. From 2018 to 2022, the water head of the Q3 and Q8 observation wells showed an upward trend, while ground subsidence showed a slowing trend (Figure 5a,e). The attenuation coefficients K were -0.52 and -0.46, respectively, and the magnitude coefficient M was 306.4 mm and 351.4 mm, respectively. The water head of the Q7, Q10, and Q18 observation wells also showed an upward trend from 2018 to 2022, but the ground subsidence rate did not show a significant slowing trend (Figure 5c,g,i), with attenuation coefficients greater than -0.1 and a magnitude coefficient M of 1832.2 mm, 1252.3 mm, and 8087.8 mm, respectively. There is no change in the groundwater level of the Q20 observation well, and the ground subsidence is accompanied by periodic slight subsidence, with a small deformation magnitude. The varied reactions of the observed aquifer systems to groundwater level shifts highlight notable disparities in the spatial distribution and thickness of aquifers and clay layers within the AOI region. Furthermore, the attenuation coefficients of ground subsidence in the entire AOI area and magnitude coefficient M were obtained, as shown in Figure 6a,b. Figure 6a clearly shows that the attenuation coefficients in the northwest Piedmont plain, the northeast Baiyangdian area, and the middle area of the south are between -1 and -0.4. There is a clear trend of slowing down ground subsidence, but in the central subsidence area, the attenuation coefficients are all greater than -0.1, and there is no trend of slowing down ground subsidence. The magnitude of the M value represents the magnitude of deformation in the aquifer at this location, where negative

values represent surface rebound (aquifer expansion) and positive values represent surface subsidence (aquifer compression). From Figure 6b, it can be seen that most of the AOI area is positive, with the maximum M value occurring at the center of the subsidence funnel, indicating that the aquifer compression is most severe here. There is no obvious trend in ground subsidence and the spatial distribution of the positive M values is consistent with the distribution of ground subsidence. The reason for this phenomenon is that crop growth requires a large amount of groundwater irrigation, leading to continuous depletion of groundwater resources and intensified ground subsidence.

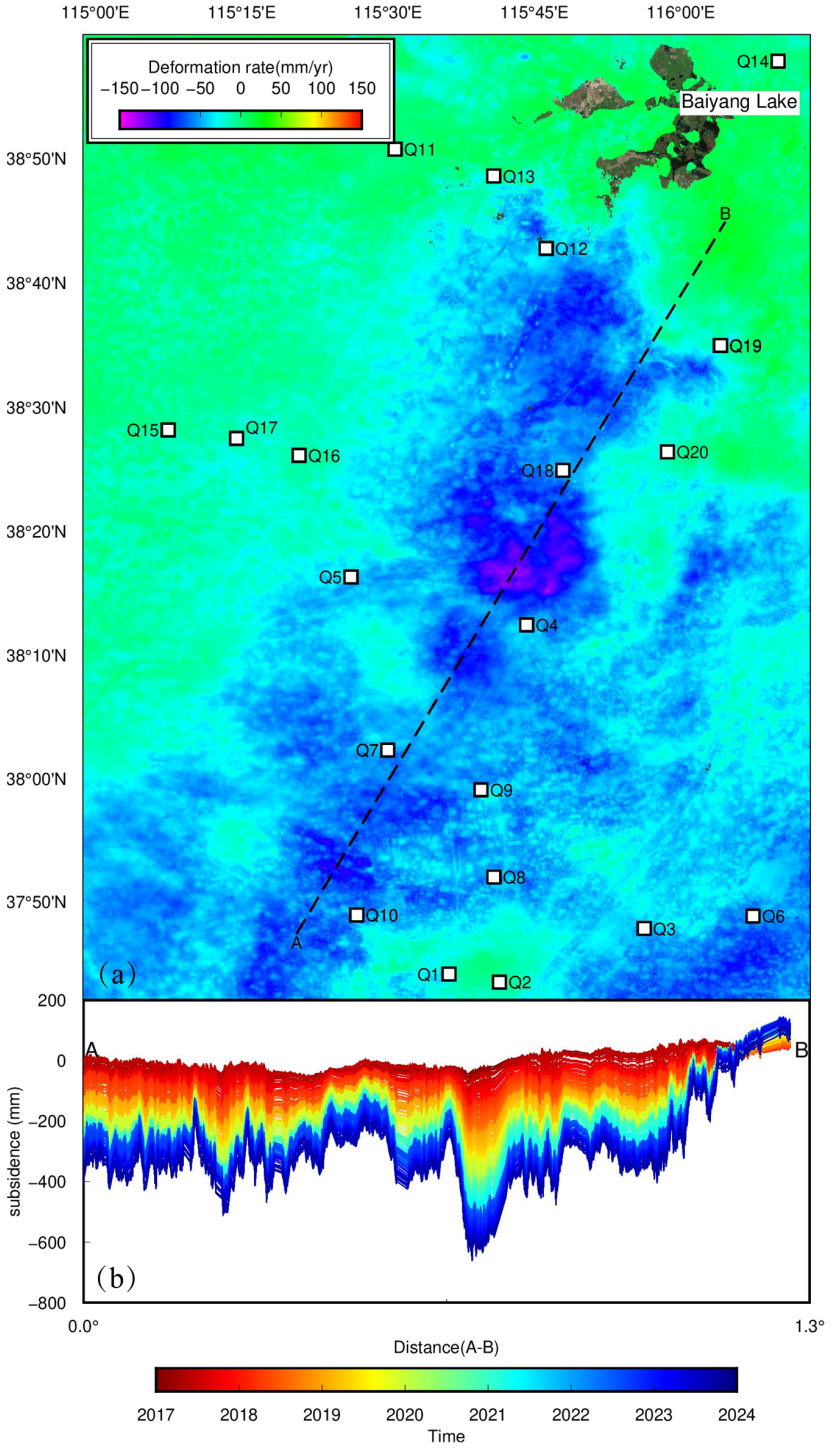

Figure 4. (**a**) The average vertical deformation rate in the AOI from 2017 to 2023, (**b**) The A-B profile results from 2017 to 2023.

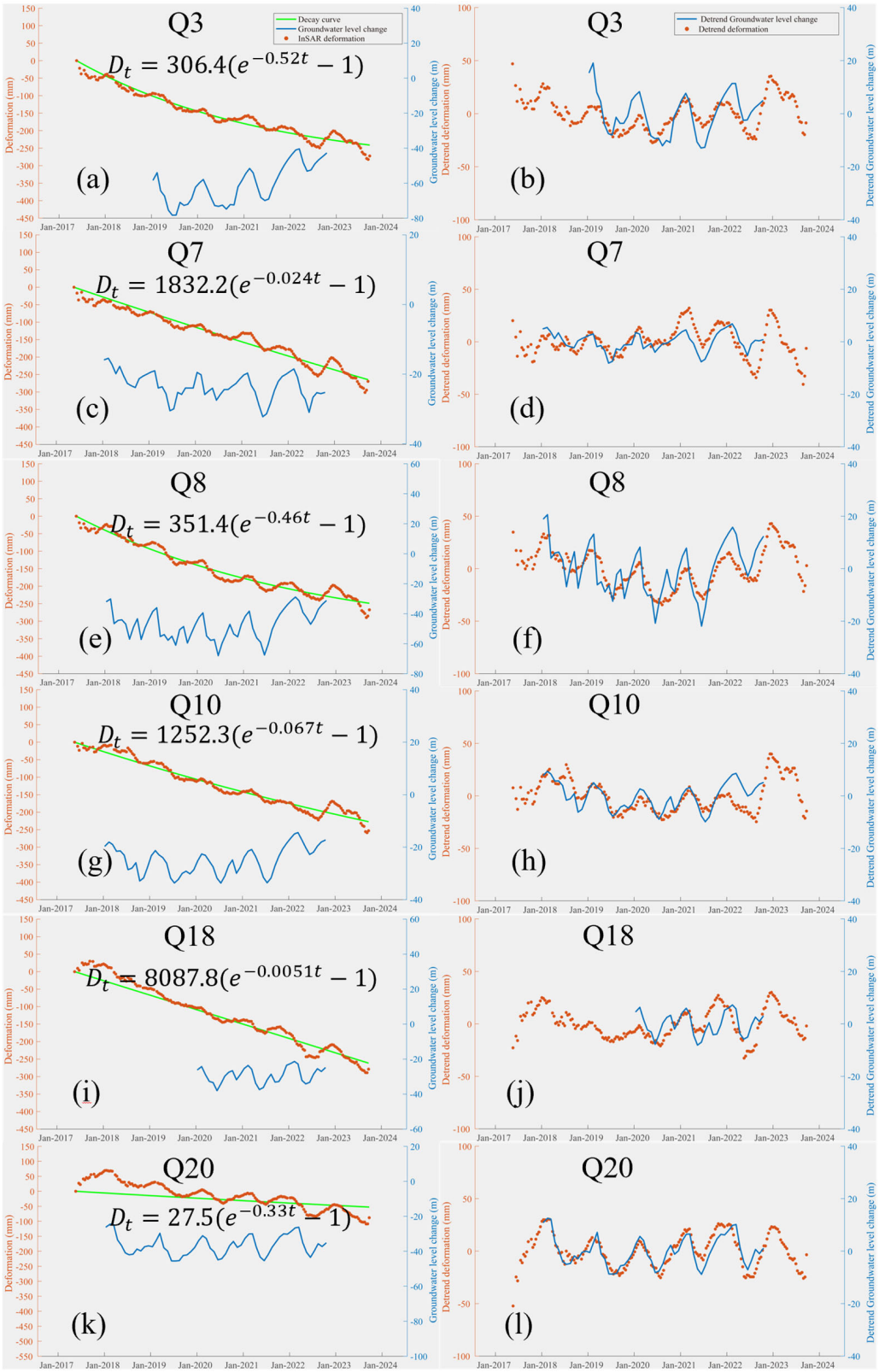

Figure 5. Groundwater level time series vs. time-series deformation for the nearby well station and detrend groundwater level time series vs. detrend time-series deformation for the nearby well station: (**a**,**b**) Q3, (**c**,**d**) Q7, (**e**,**f**) Q8, (**g**,**h**) Q10, (**i**,**j**) Q18 and (**k**,**l**) Q20.

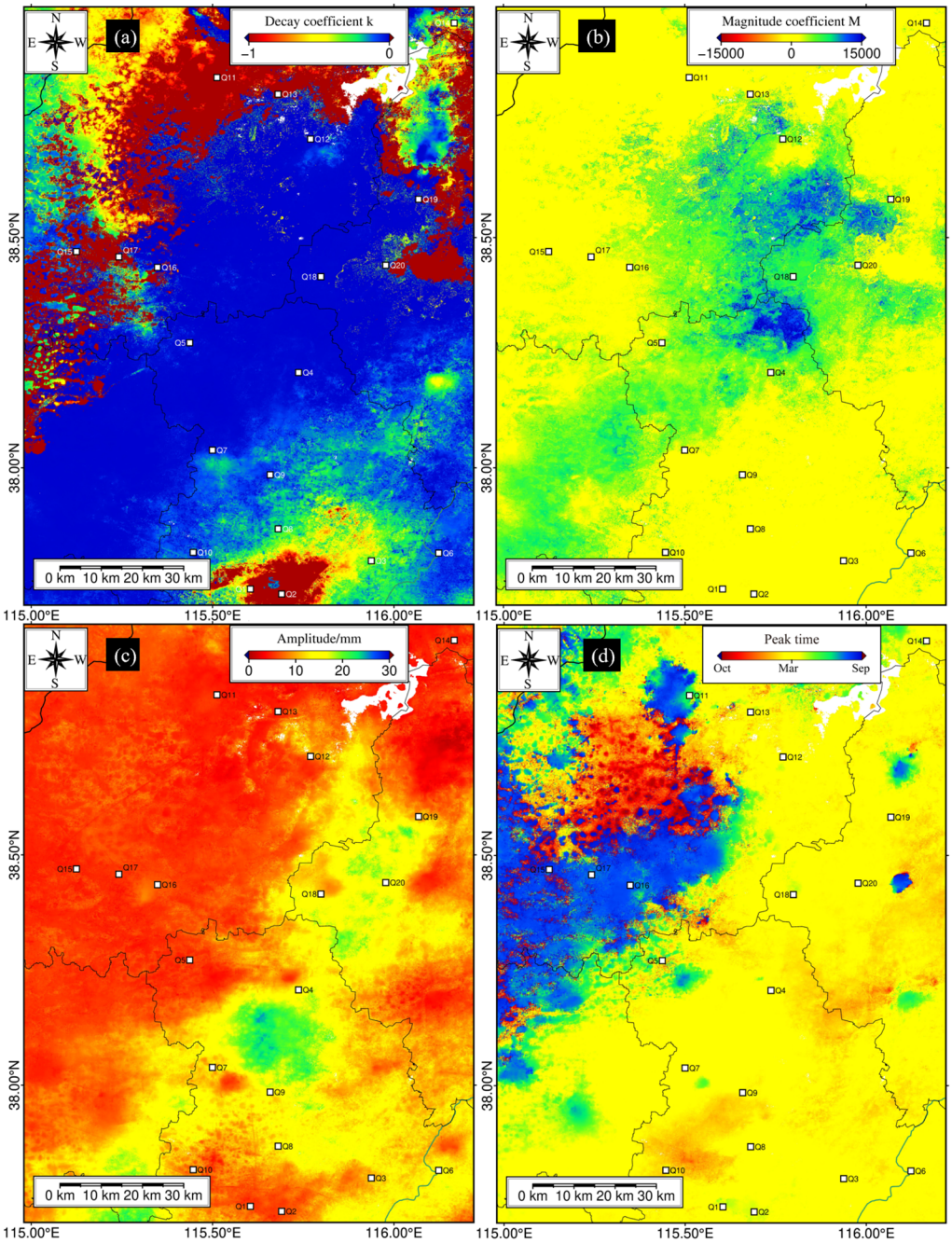

Figure 6. The map of the (k) decay coefficient (**a**) and the (M) magnitude coefficient (**b**) from long-time deformation, the (A) amplitude (**c**), and the peak time (**d**) from seasonal deformation.

4.2. Seasonal Deformation Results and Analysis

The response of the surface to seasonal changes in the groundwater level is the generation of seasonal deformation. In this article, a harmonic function is used to extract the seasonal groundwater level of typical observation wells and the seasonal deformation of nearby InSAR monitoring points, as shown in Figure 5b,d,f,h,j,l. The amplitude of seasonal deformation is about 15–30 mm, and the peak of deformation is from January to March each year. The amplitude of the seasonal water level change is about 10–20 m, and the peak time of groundwater level change is also from January to March each year. Further correlation between the groundwater level and surface deformation was conducted, and it was found that the InSAR deformation near the observation well lagged behind the groundwater level changes by about 5–192 days, as shown in Table 2. This is mainly due to the large difference

in the clay layer thickness and low permeability coefficient in the aquifer system, and the extracted groundwater level needs a period of time to reach equilibrium again. To analyze the spatiotemporal characteristics of seasonal deformation in the entire AOI region, the amplitude and peak time of seasonal deformation from 2017 to 2023 were calculated. The results showed that there was significant seasonal deformation in the central and southern subsidence areas of the AOI, with an amplitude of 15–25 mm, as shown in Figure 6c. The peak time of seasonal deformation in this subsidence area was from January to March, as shown in Figure 6d, which is consistent with changes in the groundwater level. In the natural state, the rainfall period in the NCP is concentrated in July–September of each year, and the groundwater level originally reached the maximum in August–October, which is consistent with that in the central and western regions of Figure 6d but is inconsistent with other regions, because the groundwater level change in the AOI settlement area is mainly controlled by agricultural irrigation, and the groundwater level reached the maximum in January~March of each year, and reached the minimum in June~July, which fully proves that the land subsidence in the AOI area is caused by overexploitation of groundwater.

Table 2. Estimated elastic storage coefficients, time lags and maximum correlation.

Station	Time Lag (Day)	Correlation	S_{ke} (10^{-3})	Station	Time Lag (Day)	Correlation	S_{ke} (10^{-3})
Q1	46	0.45	2.32 ± 0.033	Q11	192	0.37	6.53 ± 0.035
Q2	54	0.57	2.02 ± 0.042	Q12	33	0.64	3.24 ± 0.086
Q3	21	0.62	1.21 ± 0.031	Q13	55	0.43	2.36 ± 0.016
Q4	15	0.58	2.34 ± 0.019	Q14	129	0.39	2.65 ± 0.017
Q5	133	0.66	4.48 ± 0.036	Q15	45	0.76	15.27 ± 0.044
Q6	27	0.58	1.02 ± 0.016	Q16	61	0.57	11.04 ± 0.036
Q7	19	0.53	3.45 ± 0.035	Q17	47	0.71	13.82 ± 0.046
Q8	18	0.74	1.77 ± 0.014	Q18	23	0.67	2.42 ± 0.038
Q9	26	0.66	1.78 ± 0.099	Q19	127	0.47	5.08 ± 0.079
Q10	22	0.71	1.90 ± 0.025	Q20	5	0.88	2.69 ± 0.026

4.3. Aquifer Parameters (S_{ke}) Estimation

The elastic skeletal storage coefficients in the AOI region was estimated using the seasonal deformation and seasonal groundwater level changes. This article estimated the S_{ke} coefficients of 20 observation wells, as shown in Table 2, and obtained the distribution map of the elastic release coefficients of the entire AOI area through inverse distance weighted interpolation data processing. The estimated elastic skeletal storage coefficients of the AOI settlement area are in the range of 1.02×10^{-3}~6.53×10^{-3}, which is consistent with the elastic release coefficient obtained from previous scholars' pumping experiments (1.0×10^{-3}~8×10^{-3}) [42]. The estimated elastic release coefficient of the Q15–Q17 observation wells in the Piedmont plain is relatively high, indicating that the groundwater in the Piedmont plain is easy to recharge and has a large variation in the groundwater level. From Figure 7, it can be seen that the water release coefficient of the elastic skeleton generally increases from east to west, which may be due to the fact that the shallow groundwater in the east is saline water. In order to meet the agricultural water demand, a large amount of deep confined groundwater was extracted, resulting in a large mining thickness in the area and difficulty in replenishing the shallow surface water.

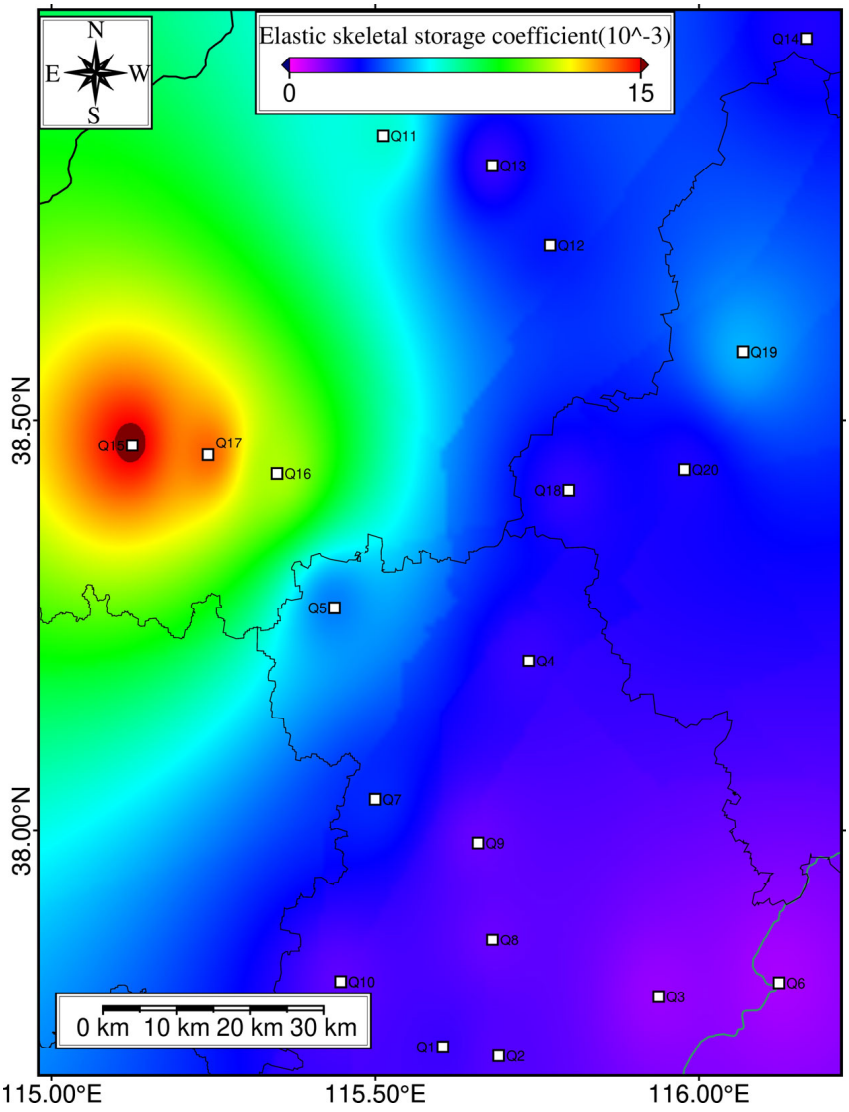

Figure 7. Interpolated S_{ke} coefficient.

4.4. GWS Parameter Estimation

This article obtained the annual TGWS parameters of the AOI region based on Formula (6), combined with the annual vertical cumulative deformation variables and the AOI region from 2018 to 2022, as shown in Figure 8. The equivalent water thickness was used to represent changes in water storage. To further explore the spatial-temporal changes in the annual TGWS, the annual average TGWS rates in the AOI area were estimated, which dropped rapidly from 48.6 mm/yr in 2018 to 13.1 mm/yr in 2022. At the same time, from Figure 8, it can be seen that the spatial distribution of the annual TGWS is shrinking sharply, and by 2022, the scope of the TGWS will only be in the settlement area in the middle of the AOI, indicating that the groundwater exploitation area and intensity are shrinking. This is due to the implementation of the SNWD project and the issuance of the groundwater exploitation policy in North China, which has enabled the agricultural irrigation area in the NCP to receive a large amount of surface water supply and deep groundwater supply, and the land subsidence has been alleviated. The above results show that the groundwater hydraulic exploitation measures have achieved good results in some areas. However, the effect is not significant in the central region where the land subsidence is serious. The main reason is that the surface water resources in this region are scarce and it is difficult to meet the water demand of this region.

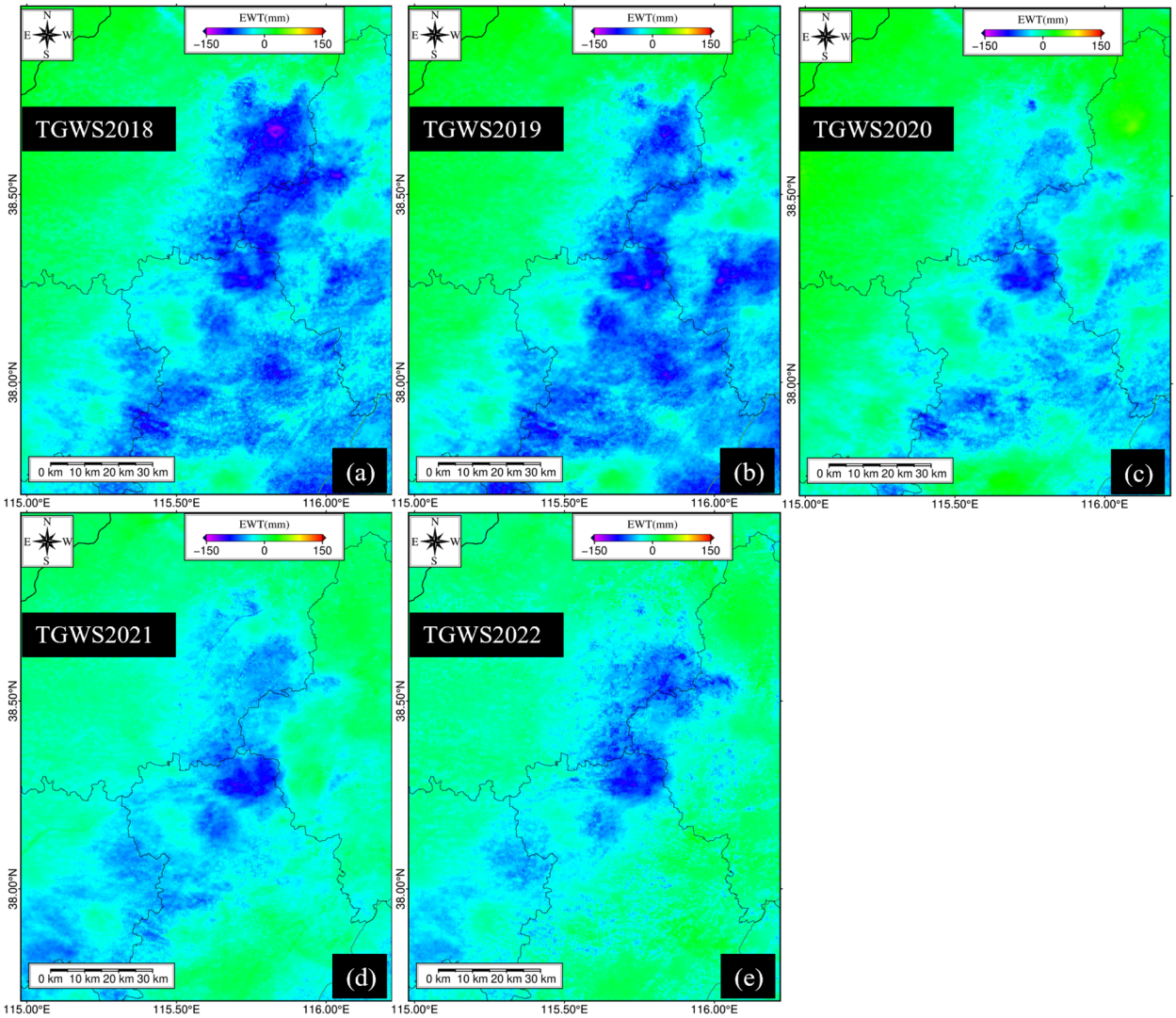

Figure 8. Annual TGWS: (**a**) 2018, (**b**) 2019, (**c**) 2020, (**d**) 2021 and (**e**) 2022.

In order to obtain the IGWS and RGWS, it was necessary to first maintain the TGWS resolution consistent with the solved S_{ke} resolution. Secondly, according to Formulas (6) and (7), the annual groundwater level changes and elastic skeleton storage coefficients (Table 2) were combined to obtain the annual IGWS and RGWS variations, as shown in Figure 9. From Figure 9a,c,e,g, it is evident that from 2018 to 2021, the RGWS parameters shifted from negative values (loss) to positive values (recovery). Further calculation was conducted on the average RGWS rate of the annual data, with an average annual RGWS loss of 11.2 mm/yr and 6.3 mm/yr during the 2018–2019 period, and an average annual RGWS recovery of 2.7 mm/yr and 10.8 mm/yr during the 2020–2021 period. During 2018–2019, the RGWS is still mainly lost, which may be caused by the low precipitation. The surface water made it difficult to meet the needs of agricultural irrigation, and the mining output of confined groundwater has increased sharply. During 2020–2021, recovery will be the main task. This phenomenon is caused by the increase in the surface water supply and rainfall in the NCP due to the SNWDP. The mining output of confined groundwater will decrease. The average annual loss rate of IGWS during the period of 2018–2021 was 34.7, 36.4, 13.6, and 8.9 mm/yr, respectively. From Figure 9b,d,f,h, it can be seen that the spatial change trend is consistent with the TGWS, both of which have a sharp decrease in the impact range. In the future, with the implementation of the South-to-North Water Diversion East Line Water Diversion Project, the IGWS may gradually disappear.

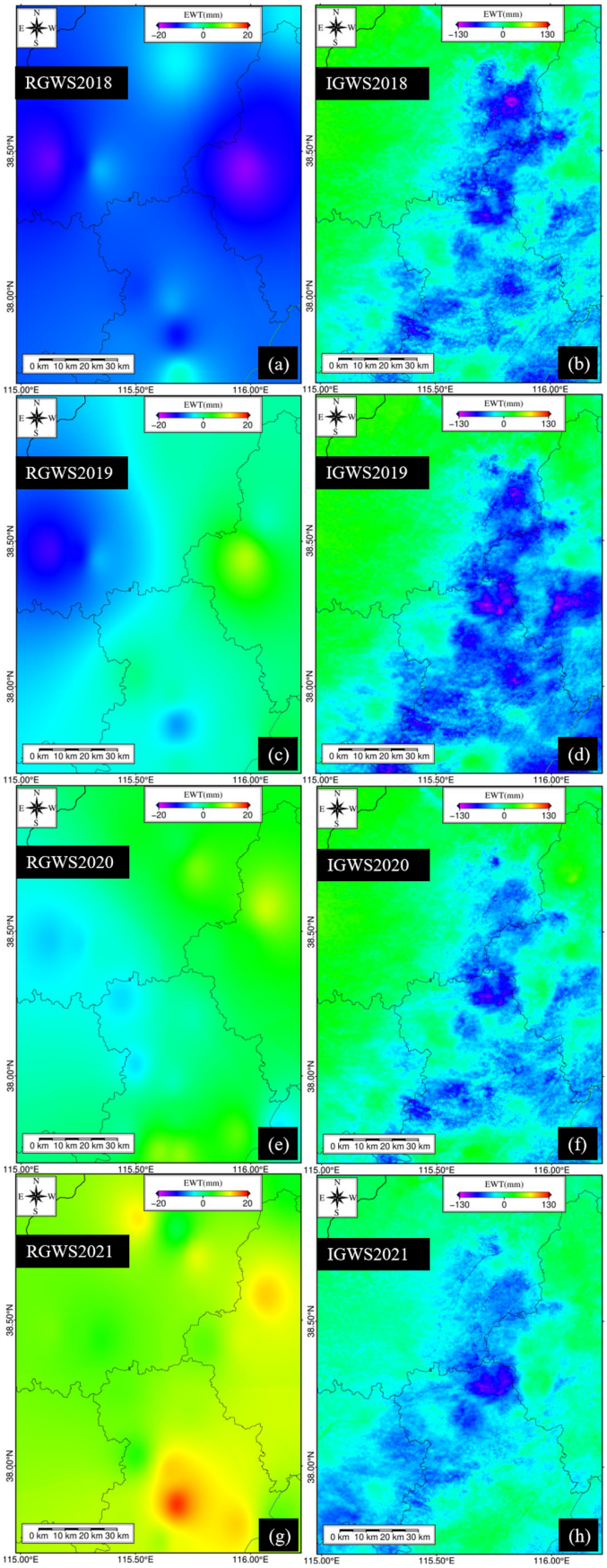

Figure 9. Annual RGWS and IGWS: (**a**,**b**) 2018, (**c**,**d**) 2019, (**e**,**f**) 2020 and (**g**,**h**) 2021.

5. Discussion

5.1. The Relationship between Heavy Rainfall and Deformation

In recent years, due to global warming, the climate in northern China has become more and more warm and humid, with frequent rainstorms in summer. On 29 July 2023, under the influence of the residual circulation of "Typhoon Dussuri", the subtropical high, the water vapor transport of "Typhoon Kanu", and the combined effect of topography, a disastrous and extremely heavy rainstorm occurred in northern Hebei Province, Beijing and surrounding areas. The precipitation in Beijing reached the highest level in 140 years of instrument measurement history, known as the "20230729" heavy rainfall event. In this study, the impact of the "20230729" heavy rainfall event on the North China Plain was emphatically analyzed, especially the temporal and spatial distribution of the surface rebound response in the short term. First, we detected and extracted the flood change through Sentinel SAR data, and we analyzed the superposition with deformation, as shown in Figure 10. The red area is the flood area, mainly flooding along the river and converging in areas with serious land subsidence. A large amount of surface water will quickly recharge the confined aquifer. In order to further quantitatively evaluate the surface rebound response, we obtained the ground deformation from 29 July 2023 to 22 September, as shown in Figure 11 Within two months, the average value of the ground uplift area has exceeded 30 mm, with the maximum ground uplift reaching 50 mm. The ground uplift extends from the middle to the east of AOI, and its magnitude also increases.

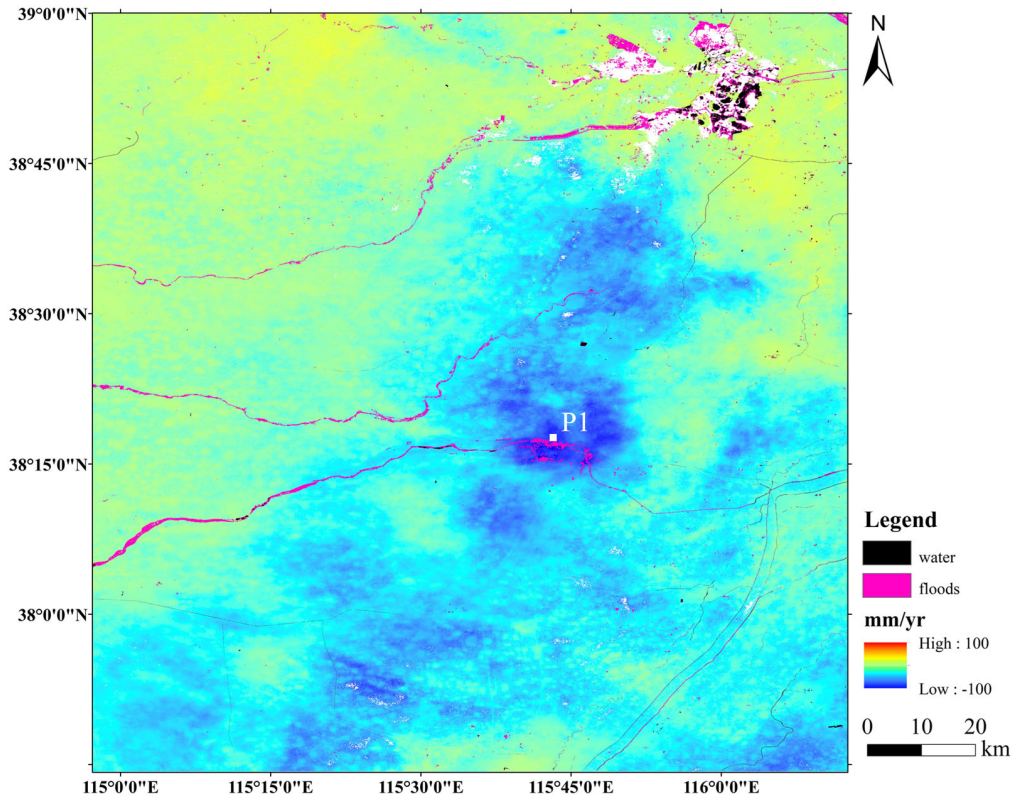

Figure 10. Flood and ground subsidence analysis.

In order to further explore the time–response relationship between the long-term rainfall and surface deformation, we selected the vertical time-series deformation data and precipitation time-series data at the center point of the subsidence funnel P1 (Figure 10) for analysis, as shown in Figure 12. The time-series deformation at P1 shows a linear settlement with periodic fluctuations, and the periodic signal is often after rainfall, which is the result of the rapid recharge of the confined aquifer by rainfall, and then the surface response. Especially with the "20210720" and "20230729" heavy rainfall events in the NCP,

the surface subsidence stops and rebounds. However, it is also worth noting that the heavy rainfall caused by the "20210720" heavy rainfall event can only delay the generation of land subsidence in the NCP but cannot eliminate land subsidence. This conclusion is consistent with previous scholarly conclusions [43]. A few months after the heavy rainfall event, land subsidence began to show a linear trend.

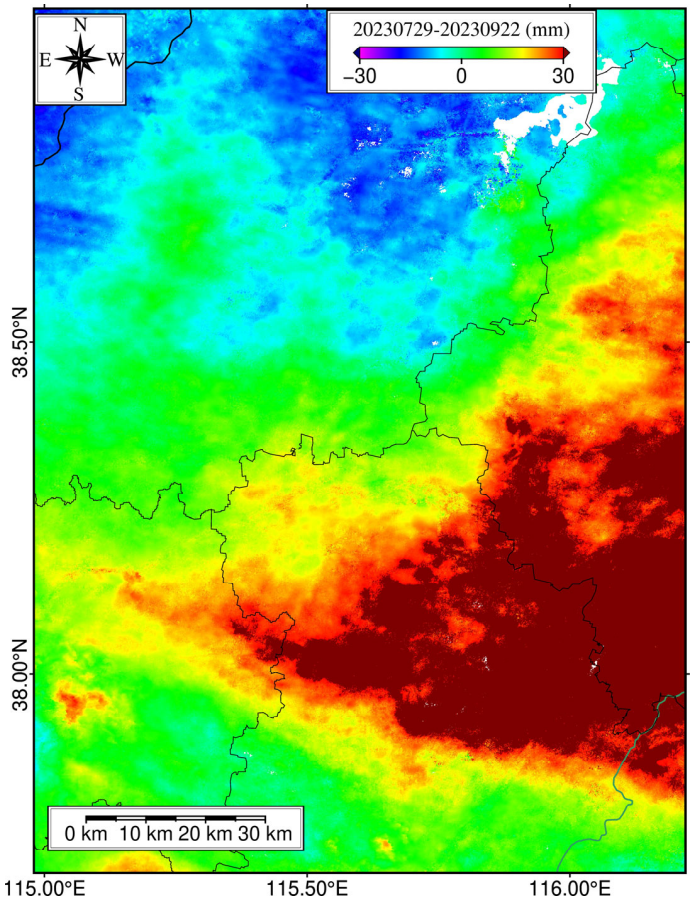

Figure 11. Surface rebound deformation map.

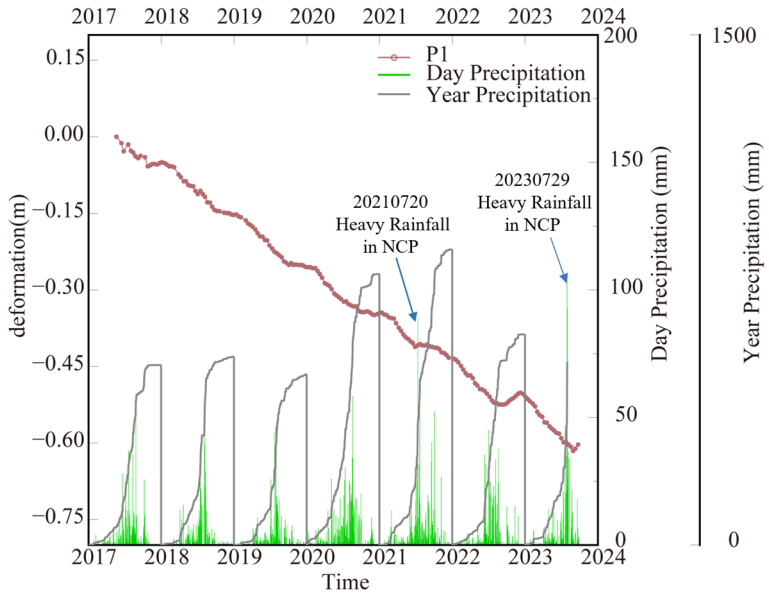

Figure 12. Correlation analysis between the times series of vertical deformation and rainfall.

5.2. Advantages and Limitations

InSAR can obtain high-resolution and long-term surface deformation fields, which can be used to analyze the spatiotemporal distribution characteristics and deformation laws of surface subsidence caused by groundwater exploitation. More and more short return period SAR satellites (e.g., Sentinel, Land Exploration One 01 Group A/B satellite (acronym LT-1A/1B), NISAR) enable us to more accurately capture the seasonal deformation and short-term surface rebound response after heavy rainfall. We can also explore the physical characteristics of groundwater changes and invert aquifer parameters by establishing a functional model between surface deformation and groundwater changes. In this paper, we used seasonal deformation data observed by InSAR and groundwater logging data to invert the elastic water release coefficient, and we further obtained the TGWS, RGWS, and IGWS parameters of the entire study area. Using InSAR to conduct inversion research on groundwater hydrological parameters can obtain high-spatial-resolution groundwater hydrological parameters, effectively addressing the problem of insufficient ground observation data and the difficulty of estimating detailed hydrological parameters in space.

However, there are still problems with using InSAR to observe and invert groundwater parameters. Firstly, the accuracy of aquifer parameter inversion still depends on the distribution density of the observed well locations. Secondly, the inversion of hydrological parameters using InSAR surface deformation data as observation values is mainly based on the Terzaghi principle-derived linear elastic model. However, in reality, in addition to linear elastic deformation, there are also plastic and viscoelastic deformations, and overly simplifying the model can lead to inaccuracies in the inversion. Thirdly, the influence of different geological structures on parameter inversion has not been considered, such as the hindering and controlling effects of faults and ground fissures on groundwater, which are also factors that must be considered in underground parameter inversion.

6. Conclusions

In this study, first, we used the MT-InSAR technology and ascending C-band Sentinel-1 SAR data from 2017 to 2023 to invest in the land deformation and analysis in the AOI area. There are multiple settling funnels in the research area, with a maximum settling rate exceeding −150 mm/yr and a cumulative deformation exceeding 600 mm. Then, we achieved the separation of periodic and long-term deformation through seasonal separation algorithms, and we modeled the long-term deformation using the exponential function model. We found that most of the settlement areas in the AOI did not show a significant trend of settlement attenuation, as only the southern region of the AOI showed settlement attenuation. Next, we used the seasonal deformation and seasonal water level to solve the S_{ke} parameters of the aquifer, with the range of 1.02×10^{-3}~6.53×10^{-3} in the subsidence areas. We further obtained the annual TGWS, RGWS, and IGWS parameters for the AOI region. From 2018 to 2021, the TGWS has been decreasing year by year, the RGWS has been increasing year by year, and the IGWS has also been rapidly decreasing. This is due to the implementation of the SNWDP water conveyance project and the issuance of the North China pressure extraction policy, which has led to a large amount of groundwater recharge for the confined aquifer. Finally, by analyzing the relationship between heavy rainfall and land deformation, we concluded that heavy rainfall can make land subsidence stop and rebound in a short time, but it can only delay the generation of land subsidence rather than eliminate land subsidence. A few months after the heavy rainfall event, the land subsidence starts to show a linear trend, so the main reason for controlling land subsidence in the NCP is the intensity of groundwater overexploitation. Our data have improved our comprehension of the groundwater storage changes in the NCP. This information aids in managing these resources scientifically and helps prevent and mitigate ground subsidence disasters.

Author Contributions: Methodology, Q.Y., X.Z., R.G. and J.H.; software, Q.Y., X.Z. and R.G.; formal analysis, Q.Y.; resources, Q.Y. and R.G.; writing—original draft, Q.Y.; writing—review and editing, R.G., X.Z. and L.Y. All authors have read and agreed to the published version of the manuscript.

Funding: This work was supported by the National Natural Science Foundation of China under Grants 42030112 and 42201432, and by the Technology and Fundamental Research Funds for the Central Universities of Central South University under Grant 2020zzts190.

Data Availability Statement: The data presented in this study are available from the corresponding author upon request.

Acknowledgments: The authors would like to thank the European Space Agency (ESA) for providing the Sentinel-1 data. The authors would like to thank the China Geological Environment Monitoring Institute GeoCloud (https://geocloud.cgs.gov.cn) for providing the groundwater data. The authors would like to thank Qing Yang for providing the flood change detection results. The authors would like to thank the National Centers for Environmental Information website (https://www.ncei.noaa.gov/maps-and-geospatial-products, accessed on 15 November 2023) for providing the precipitation records.

Conflicts of Interest: The authors declare no conflicts of interest.

References

1. Herrera-Garcia, G.; Ezquerro, P.; Tomas, R.; Bejar-Pizarro, M.; Lopez-Vinielles, J.; Rossi, M.; Mateos, R.M.; Carreon-Freyre, D.; Lambert, J.; Teatini, P.; et al. Mapping the global threat of land subsidence. *Science* **2021**, *371*, 34–36. [CrossRef]
2. Jeanne, P.; Farr, T.G.; Rutqvist, J.; Vasco, D.W. Role of agricultural activity on land subsidence in the San Joaquin Valley, California. *J. Hydrol.* **2019**, *569*, 462–469. [CrossRef]
3. Hoffmann, J.; Galloway, D.L.; Zebker, H.A. Inverse modeling of interbed storage parameters using land subsidence observations, Antelope Valley, California. *Water Resour. Res.* **2003**, *39*, 1031. [CrossRef]
4. Amelung, C.C. Land subsidence in central Mexico detected by ALOS InSAR time-series. *Remote Sens. Environ.* **2014**, *140*, 94–106.
5. Motagh, M.; Shamshiri, R.; Haghighi, M.H.; Wetzel, H.-U.; Akbari, B.; Nahavandchi, H.; Roessner, S.; Arabi, S. Quantifying groundwater exploitation induced subsidence in the Rafsanjan plain, southeastern Iran, using InSAR time-series and in situ measurements. *Eng. Geol.* **2017**, *218*, 134–151. [CrossRef]
6. Halipu, A.; Wang, X.; Iwasaki, E.; Yang, W.; Kondoh, A. Quantifying Water Consumption through the Satellite Estimation of Land Use/Land Cover and Groundwater Storage Changes in a Hyper-Arid Region of Egypt. *Remote Sens.* **2022**, *14*, 2608. [CrossRef]
7. Zhang, Y.; Wu, J.; Xue, Y.; Wang, Z.; Yao, Y.; Yan, X.; Wang, H. Land subsidence and uplift due to long-term groundwater extraction and artificial recharge in Shanghai, China. *Hydrogeol. J.* **2015**, *23*, 1851–1866. [CrossRef]
8. Zhang, X.; Cheng, Z.; Xu, B.; Gui, R.; Hu, J.; Yang, C.; Yang, Q.; Xiong, T. Coupling the Relationship between Land Subsidence and Groundwater Level, Ground Fissures in Xi'an City Using Multi-Orbit and Multi-Temporal InSAR. *Remote Sens.* **2023**, *15*, 3567. [CrossRef]
9. Zhu, K.; Zhang, X.; Sun, Q.; Wang, H.; Hu, J. Characterizing Spatiotemporal Patterns of Land Deformation in the Santa Ana Basin, Los Angeles, from InSAR Time Series and Independent Component Analysis. *Remote Sens.* **2022**, *14*, 2624. [CrossRef]
10. Gong, H.; Pan, Y.; Zheng, L.; Li, X.; Zhu, L.; Zhang, C.; Huang, Z.; Li, Z.; Wang, H.; Chaofan, Z. Long-term groundwater storage changes and land subsidence development in the North China Plain (1971–2015). *Hydrogeol. J.* **2018**, *26*, 1417–1427. [CrossRef]
11. Shi, M.; Gong, H.; Gao, M.; Chen, B.; Zhou, C. Recent Ground Subsidence in the North China Plain, China, Revealed by Sentinel-1A Datasets. *Remote Sens.* **2020**, *12*, 3579. [CrossRef]
12. Wang, L.; Jia, B.; Xie, Z.; Wang, B.; Liu, S.; Li, R.; Liu, B.; Wang, Y.; Chen, S. Impact of groundwater extraction on hydrological process over the Beijing-Tianjin-Hebei region, China. *J. Hydrol.* **2022**, *609*, 127689. [CrossRef]
13. Dong, J.; Lai, S.; Wang, N.; Wang, Y.; Zhang, L.; Liao, M. Multi-scale deformation monitoring with Sentinel-1 InSAR analyses along the Middle Route of the South-North Water Diversion Project in China. *Int. J. Appl. Earth Obs. Geoinf.* **2021**, *100*, 102324. [CrossRef]
14. Zhang, K.; Ge, L.; Li, X.; Ng, A.H.-M. Monitoring ground surface deformation over the North China Plain using coherent ALOS PALSAR differential interferograms. *J. Geod.* **2013**, *87*, 253–265. [CrossRef]
15. Xiao, R.; Yu, C.; Li, Z.; Song, C.; He, X. General survey of large-scale land subsidence by GACOS-corrected InSAR stacking: Case study in North China Plain. *Proc. Int. Assoc. Hydrol. Sci.* **2020**, *382*, 213–218. [CrossRef]
16. Su, G.; Wu, Y.; Zhan, W.; Zheng, Z.; Chang, L.; Wang, J. Spatiotemporal evolution characteristics of land subsidence caused by groundwater depletion in the North China plain during the past six decades. *J. Hydrol.* **2021**, *600*, 126678. [CrossRef]
17. Gerald, W.; Bawden, W.T.; Stein, R.S.; Hudnut, K.W.; Peltzer, G. Tectonic contraction across Los Angeles after removal of groundwater pumping effects. *Nature* **2001**, *412*, 812–815.
18. Shi, G.; Ma, P.; Hu, X.; Huang, B.; Lin, H. Surface response and subsurface features during the restriction of groundwater exploitation in Suzhou (China) inferred from decadal SAR interferometry. *Remote Sens. Environ.* **2021**, *256*, 112327. [CrossRef]

19. Amelung, F.; Galloway, D.L.; Bell, J.W.; Zebker, H.A.; Laczniak, R.J. Sensing the ups and downs of Las Vegas: InSAR reveals structural control of land subsidence and aquifer-system deformation. *Geology* **1999**, *27*, 483–486. [CrossRef]
20. Chaussard, E.; Bürgmann, R. Remote Sensing of Ground Deformation for Monitoring Groundwater Management Practices: Application to the Santa Clara Valley During the 2012-2015 California Drought: Groundwater Monitoring With InSAR. *J. Geophys. Res. Solid Earth* **2017**, *122*, 8566–8582. [CrossRef]
21. Chaussard, E.; Bürgmann, R.; Shirzaei, M.; Fielding, E.J.; Baker, B. Predictability of hydraulic head changes and characterization of aquifer-system and fault properties from InSAR-derived ground deformation. *J. Geophys. Res. Solid Earth* **2014**, *119*, 6572–6590. [CrossRef]
22. Hoffmann, J.R.; Zebker, H.A.; Galloway, D.L.; Amelung, F. Seasonal subsidence and rebound in Las Vegas Valley, Nevada, observed by Synthetic Aperture Radar Interferometry. *Water Resour. Res.* **2001**, *37*, 1551–1566. [CrossRef]
23. Hu, X.; Bürgmann, R. Aquifer deformation and active faulting in Salt Lake Valley, Utah, USA. *Earth Planet. Sci. Lett.* **2020**, *547*, 116471. [CrossRef]
24. Shi, X.; Zhu, T.; Tang, W.; Jiang, M.; Jiang, H.; Yang, C.; Zhan, W.; Ming, Z.; Zhang, S. Inferring decelerated land subsidence and groundwater storage dynamics in Tianjin–Langfang using Sentinel-1 InSAR. *Int. J. Digit. Earth* **2022**, *15*, 1526–1546. [CrossRef]
25. Peng, M.; Lu, Z.; Zhao, C.; Motagh, M.; Bai, L.; Conway, B.D.; Chen, H. Mapping land subsidence and aquifer system properties of the Willcox Basin, Arizona, from InSAR observations and independent component analysis. *Remote Sens. Environ.* **2022**, *271*, 112894. [CrossRef]
26. Pride, S.R.; Vasco, D.W.; Flekkoy, E.G.; Holtzman, R. Dispersive transport and symmetry of the dispersion tensor in porous media. *Phys. Rev. E* **2017**, *95*, 043103. [CrossRef] [PubMed]
27. Smith, R.G.; Hashemi, H.; Chen, J.; Knight, R. Apportioning deformation among depth intervals in an aquifer system using InSAR and head data. *Hydrogeol. J.* **2021**, *29*, 2475–2486. [CrossRef]
28. Galloway, D.L.; Burbey, T.J. Review: Regional land subsidence accompanying groundwater extraction. *Hydrogeol. J.* **2011**, *19*, 1459–1486. [CrossRef]
29. Galloway, D.L.; Hudnut, K.W.; Ingebritsen, S.E.; Phillips, S.P.; Peltzer, G.; Rogez, F.; Rosen, P.A. Detection of aquifer system compaction and land subsidence using interferometric synthetic aperture radar, Antelope Valley, Mojave Desert, California. *Water Resour. Res.* **1998**, *34*, 2573–2585. [CrossRef]
30. Qu, F.; Lu, Z.; Zhang, Q.; Bawden, G.W.; Kim, J.-W.; Zhao, C.; Qu, W. Mapping ground deformation over Houston–Galveston, Texas using multi-temporal InSAR. *Remote Sens. Environ.* **2015**, *169*, 290–306. [CrossRef]
31. Su, G.; Xiong, C.; Zhang, G.; Wang, Y.; Shen, Q.; Chen, X.; An, H.; Qin, L. Coupled processes of groundwater dynamics and land subsidence in the context of active human intervention, a case in Tianjin, China. *Sci. Total Environ.* **2023**, *903*, 166803. [CrossRef]
32. Chen, M.; Tomás, R.; Li, Z.; Motagh, M.; Li, T.; Hu, L.; Gong, H.; Li, X.; Yu, J.; Gong, X. Imaging Land Subsidence Induced by Groundwater Extraction in Beijing (China) Using Satellite Radar Interferometry. *Remote Sens.* **2016**, *8*, 468. [CrossRef]
33. Yu, X.; Wang, G.; Hu, X.; Liu, Y.; Bao, Y. Land subsidence in Tianjin, China: Before and after the south-to-north water diversion. *Remote Sens.* **2023**, *15*, 1647. [CrossRef]
34. Zhang, S.; Zhang, Y.; Yu, J.; Fan, Q.; Si, J.; Zhu, W.; Song, M. Interpretation of the Spatiotemporal Evolution Characteristics of Land Deformation in Beijing during 2003–2020 Using Sentinel, ENVISAT, and Landsat Data. *Remote Sens.* **2022**, *14*, 2242. [CrossRef]
35. Falabella, F.; Serio, C.; Masiello, G.; Zhao, Q.; Pepe, A. A Multigrid InSAR Technique for Joint Analyses at Single-Look and Multi-Look Scales. *IEEE Geosci. Remote Sens. Lett.* **2022**, *19*, 4014905. [CrossRef]
36. Lauknes, T.R.; Zebker, H.A.; Larsen, Y. InSAR Deformation Time Series Using an L_1-Norm Small-Baseline Approach. *IEEE Trans. Geosci. Remote Sens.* **2010**, *49*, 536–546. [CrossRef]
37. Hooper, A.; Segall, P.; Zebker, H. Persistent scatterer interferometric synthetic aperture radar for crustal deformation analysis, with application to Volcán Alcedo, Galápagos. *J. Geophys. Res. Solid Earth* **2007**, *112*(B7). [CrossRef]
38. Yu, C.; Li, Z.; Penna, N.T. Interferometric synthetic aperture radar atmospheric correction using a GPS-based iterative tropospheric decomposition model. *Remote Sens. Environ.* **2018**, *204*, 109–121. [CrossRef]
39. Jiang, L.; Bai, L.; Zhao, Y.; Cao, G.; Wang, H.; Sun, Q. Combining InSAR and Hydraulic Head Measurements to Estimate Aquifer Parameters and Storage Variations of Confined Aquifer System in Cangzhou, North China Plain. *Water Resour. Res.* **2018**, *54*, 8234–8252. [CrossRef]
40. Terzaghi, K. Principles of soil mechanics: IV Settlement and consolidation of clay. *Eng. News-Rec.* **1925**, *95*, 874–878.
41. Miller, M.M.; Shirzaei, M. Spatiotemporal characterization of land subsidence and uplift in Phoenix using InSAR time series and wavelet transforms. *J. Geophys. Res. Solid Earth* **2015**, *120*, 5822–5842. [CrossRef]
42. Zhaoji, Z.; Yuhong, F.; Zongyu, C.; Zongzhuang, Z.; Zhenhua, X.; Yabin, W.; Jinxiang, M.; Lizhi, Y.; Jingli, S.; Menggui, J. *Investigation and Evaluation of Sustainable Utilization of Groundwater in North China Plain*; Geological Publishing House: Beijing, China, 2009.
43. Murray, K.D.; Lohman, R.B. Short-lived pause in Central California subsidence after heavy winter precipitation of 2017. *Sci. Adv.* **2018**, *4*, eaar8144. [CrossRef] [PubMed]